Weak Lensing with SDSS Commissioning Data: The Galaxy-Mass Correlation Function To $1h^{-1}$ Mpc

Philippe Fischer[1], Timothy A. McKay[2], Erin Sheldon[2], Andrew Connolly[3], Albert Stebbins[4], Joshua A. Frieman[4,5], Bhuvnesh Jain[6], Michael Joffre[5], David Johnston[5], Gary, Bernstein[1], James Annis[4], Neta A. Bahcall[7], J. Brinkmann[9], Michael A. Carr[7], István Csabai[6,10], James E. Gunn[7], G. S. Hennessy[11], Robert B. Hindsley[11], Charles Hull[12], Željko Ivezić[7], G. R. Knapp[7], Siriluk Limmongkol[13], Robert H. Lupton[7], Jeffrey A. Munn[14], Thomas Nash[4], Heidi Jo Newberg[15], Russell Owen[13], Jeffrey R. Pier[14], Constance M. Rockosi[5], Donald P. Schneider[8], J. Allyn Smith[2], Chris Stoughton[4], Alexander S. Szalay[6], Gyula P. Szokoly[6], Aniruddha R Thakar[6], Michael S. Vogeley[16], Patrick Waddell[13], David H. Weinberg[17], Donald G. York[5], (the SDSS Collaboration)

ABSTRACT

We present measurements of galaxy-galaxy weak lensing from 225 square degrees of early commissioning imaging data from the Sloan Digital Sky Survey (SDSS). We measure a mean tangential shear around a stacked sample of foreground galaxies in three bandpasses (g', r', and i') out to angular radii of $600''$, detecting the shear signal at very high statistical significance. The shear profile is well described by a power law $\gamma_T = \gamma_{T0}(1'/\theta)^{\eta}$, with best fit slope of $\eta = 0.7 - 1.1$ (95% confidence). In the range $\theta = 10'' - 600''$, the mean tangential shear is approximately $6 \pm 1 \times 10^{-4}$ in all three bands. A variety of rigorous tests demonstrate the reality of the gravitational lensing signal and confirm the uncertainty estimates. In particular, we obtain shear measurements

[1]University of Michigan, Department of Astronomy, 830 Dennison Building, Ann Arbor, MI 48109

[2]University of Michigan, Department of Physics, 500 East University, Ann Arbor, MI 48109

[3]Department of Physics and Astronomy, University of Pittsburgh, Pittsburgh PA 15260

[4]Fermi National Accelerator Laboratory, P.O. Box 500, Batavia, IL 60510

[5]University of Chicago, Astronomy & Astrophysics Center, 5640 S. Ellis Ave., Chicago, IL 60637

[6]Department of Physics and Astronomy, The Johns Hopkins University, 3701 San Martin Drive, Baltimore, MD 21218, USA

[7]Princeton University Observatory, Princeton, NJ 08544

[8]Department of Astronomy and Astrophysics, The Pennsylvania State University, University Park, PA 16802

[9]Apache Point Observatory, P.O. Box 59, Sunspot, NM 88349-0059

[10]Department of Physics of Complex Systems, Eötvös University, Pázmány Péter sétány 1/A, Budapest, H-1117, Hungary

[11]U.S. Naval Observatory, 3450 Massachusetts Ave., NW, Washington, DC 20392-5420

[12]The Observatories of the Carnegie Institution of Washington, 813 Santa Barbara St, Pasadena, CA 91101

[13]University of Washington, Department of Astronomy, Box 351580, Seattle, WA 98195

[14]U.S. Naval Observatory, Flagstaff Station, P.O. Box 1149, Flagstaff, AZ 86002-1149

[15]Dept. of Physics, Applied Physics and Astronomy Rensselaer Polytechnic Institute Troy, NY 12180

[16]Department of Physics Drexel University Philadelphia, PA 19104

[17]Ohio State University, Dept. of Astronomy, 174 W. 18th Ave., Columbus, OH 43210

consistent with zero when we rotate the background galaxies by 45°, replace foreground galaxies with random points, or replace foreground galaxies with bright stars. We interpret our results by assuming that all matter correlated with galaxies belongs to the galaxies. We model the mass distributions of the foreground galaxies, which have a mean luminosity $\langle L(\theta < 5'') \rangle = 8.7 \pm 0.7 \times 10^9 h^{-2}$ $L_{g'\odot}$, $1.4 \pm 0.12 \times 10^{10} h^{-2}$ $L_{r'\odot}$, $1.8 \pm 0.14 \times 10^{10} h^{-2}$ $L_{i'\odot}$, as approximately isothermal spheres characterized by a velocity dispersion σ_v and a truncation radius s. The velocity dispersion is constrained to be $\sigma_v = 150 - 190$ km s^{-1} at 95% confidence ($145 - 195$ km s^{-1} including systematic uncertainties), consistent with previous determinations but with smaller error bars. Our detection of shear at large angular radii sets a 95% confidence lower limit $s > 140''$, corresponding to a physical radius of $260 h^{-1}$ kpc, implying that the dark halos of typical luminous galaxies extend to very large radii. However, it is likely that this is being systematically biased to large value by diffuse matter in the halos of groups and clusters of galaxies. We also present a preliminary determination of the galaxy-mass correlation function finding a correlation length similar to the galaxy autocorrelation function and consistency with a low matter density universe with modest bias.

The full SDSS will cover an area 44 times larger and provide spectroscopic redshifts for the foreground galaxies, making it possible to greatly improve the precision of these constraints, to measure additional parameters such as halo shape and halo concentration, and to measure the properties of dark matter halos separately for many different classes of galaxies.

Subject headings: dark matter — gravitational lensing — large-scale structure of universe — galaxies: fundamental parameters — galaxies: halos

1. Introduction

According to the theory of General Relativity, matter in the universe will deflect rays of light. The consequence of this is that if one observes objects located behind mass concentrations the background objects will appear magnified, distorted and sometimes multiply imaged. This phenomenon, known as gravitational lensing, can be used to measure the mass distributions of the foreground objects. Mass measurements made in this manner are direct, and hence free of the model-dependent biases of dynamical mass measurements.

Multiple imaging, strong distortions and large magnifications occur when the light rays pass near very high mass density regions, and is referred to as strong gravitational lensing. Regions which produce strong lensing are usually near the centers of galaxies or clusters of galaxies. At larger impact parameter, the distortions and magnifications are much smaller and multiple images do not occur; this is known as the weak lensing regime. By studying the small distortions in the background galaxies one can measure mass distributions out to very large radii. Weak gravitational lensing has been successfully used to measure mass distributions of clusters of galaxies (see the recent review by Mellier (1999)) and somewhat less successfully to measure halos of galaxies (Tyson et al. 1984; Brainerd et al. 1996; Dell'Antonio & Tyson 1996; Griffiths, Casertano, Im, & Ratnatunga 1996; Hudson, Gwyn, Dahle & Kaiser 1998). The problem in the latter case (known as galaxy-galaxy lensing) is that an individual galaxy produces only a very small distortion in the background galaxies. Since the background galaxies are intrinsically elliptical the lensing signal is small compared to the "shape noise". Therefore, one needs to average the distortion behind many background galaxies, which requires a large observed field.

The Sloan Digital Sky Survey (SDSS) will image 10000 square degrees in five bandpasses. Although the images will be relatively shallow compared to many previous weak lensing studies, they are, as we will show in this paper, well suited to a galaxy-galaxy lensing study. Advantages of using brighter galaxies include better known redshift distributions and larger angular size. The latter means that the seeing requirements are less stringent than for studies based on faint galaxies.

In this paper we report on a weak lensing study done with two nights of SDSS commissioning data

covering approximately 225 square degrees. We detect highly significant weak lensing signals in the g', r' and i' bandpasses. In §2 we give details of the observations, in §3 we discuss our methods for analyzing the data including correcting for PSF anisotropy (§3.1), shear measurement (§3.2), and galaxy redshift estimation (§3.4). In §4 we list sources of random and systematic error and in §4.3 we discuss tests of the significance of the shear measurements. In §5 we model the data and we present the discussion and conclusions in §6 and §7. Throughout this paper we use $h = \mathrm{H}_0/100$ km s^{-1} and assume $\Omega = 1$.

2. Observations

The SDSS 2.5m telescope is described by Siegmund et al (2000) (see also http://www.astro.princeton.edu/PBOOK/telescop/telescop.htm). The telescope provides a nearly 3°, virtually undistorted field of view. The SDSS imaging camera (Gunn et al 1998; Doi, M. et al. 2000) is a mosaic of 30 2048×2048 pixel CCDs used for the primary imaging, along with an additional 24 500x2048 CCDs used for astrometric and focus measurements. The imaging CCDs are arranged in six columns of 5 CCDs each. Each of the 5 CCDs in a column views the sky through a different broadband filter. The five filters (u', g', r', i', z') (Fukugita et al. 1996) span a range from the atmospheric cutoff at 300nm to the limit of CCD sensitivity at 1100nm. Pixels in the imaging camera subtend 0.396″ on the sky. Details of the data acquisition, reduction and calibration can be found in Petravick et al. (2000); Uomoto et al. (2000); Kent et al. (2000); Pier et al. (2000); Tucker et al. (2000).

SDSS imaging data are obtained in drift scan mode. In general, the telescope is driven along a great circle on the sky in such a way that objects pass directly down a column of CCDs. This allows essentially simultaneous observations to be obtained in each of the five passbands and provides very efficient survey observing (the shutter never closes). Total integration time in each filter is 54.1s. Because the CCD columns are separated by nearly a CCD width, a single SDSS observation of a strip of sky contains large gaps. The gaps in a single "strip" are then filled in on a subsequent night to obtain a completely filled "stripe". Successful drift scanning with a wide field system requires an optical design with very low distortion, which has the added benefit of removing an important shape systematic present for many other lensing studies.

The observations analyzed here consist of two nights of SDSS commissioning data taken 20-21 March 1999 (SDSS runs 752 and 756). The total observation time was seven hours the first night and eight hours the second night. These observations were taken in a simplified mode in which the telescope remains parked at the celestial equator. Atmospheric seeing averaged 1.5″ (FWHM) the first night and 1.25″ the second night. The RMS sky noise for these data averages 26.0, 25.5 and 25.0 mag per square arcsec for g', r' and i', respectively.

The portion of the data used in this analysis is a rectangle with corners (RA, Dec.) = (9:40, -1:16) and (15:46, 1:16) (J2000) for a total of approximately 225 square degrees. Since the system sensitivity in u' and z' is relatively low, only g', r' and i' are used for determining the galaxy-galaxy lensing signal. The galaxy photometry was dereddened using the extinction values from Schlegel et al. (1998).

The photometric calibration used in this paper is only accurate to 5–10%, due to systematics in the shape of the point spread function across individual CCDs, and the fact that the primary standard star network had not yet been finalized at the time of these observations. This situation will be improved to the survey requirement of 2% in the near future. Thus we denote the preliminary SDSS magnitudes presented here as u^*, g^*, r^*, i^* and z^*, rather than the notation u', g', r', i' and z' that will be used for the final SDSS photometry.

3. Analysis

Weak lensing studies require accurate galaxy shape measurement for gravitational shear estimation (see §3.2). The standard SDSS pipeline software, outputs a plethora of parameters for each detected object (Lupton et al. 2000) including accurate coordinates and photometry. For this paper, we reprocess the data in order to measure galaxy shapes optimally as outlined in Bernstein et al. (2000), which produces object (galaxy and star) shapes and uncertainties. In order to do this, object coordinates and sizes are taken from the pipeline output as starting guesses. We then measure quadratic moments (Q_{ij}) of the surface brightness distributions weighted by an elliptical Gaussian of location, size and orientation matched (through an iterative procedure) to that of the object being measured:

$$Q_{ij} = \sum_{k,l} I_{k,l} G_{k,l} x_i x_j, \tag{1}$$

where $I_{k,l}$ is the sky-subtracted surface brightness of pixel (k,l), $G_{k,l}$ is the value of the adaptively matched elliptical Gaussian and x_i is the pixel coordinate in the centroid-subtracted coordinate system. From the quadratic moments one obtains the object ellipticities (e.g., Kaiser et al. (1995)):

$$e_1 = \frac{Q_{11} - Q_{22}}{Q_{11} + Q_{22}}, \tag{2}$$

$$e_2 = \frac{2Q_{12}}{Q_{11} + Q_{22}}. \tag{3}$$

3.1. Correcting Galaxy Shapes

The commissioning data used in this analysis were taken when the telescope was not well collimated. Therefore, the image quality is relatively poor; the PSFs are not radially symmetric and they vary strongly with both time and position in the camera. This PSF anisotropy biases the shapes of galaxies. We attempt to correct for anisotropic PSFs in the following manner. First we characterize the PSFs in small regions spanning $600'' \times 800''$ by fitting second order polynomials in R.A. and Dec. to the quadratic moments of stars. We use stars with limiting magnitudes of 21, 20, and 19 (g', r' and i'). We then interpolate the polynomials at the positions of galaxies and correct the measured galaxy shapes:

$$e_i(true) = e_i(measured) - S_{Sm} \times e_i(star), \tag{4}$$

where S_{Sm} is the smear polarizability (Kaiser et al. 1995; Bernstein et al. 2000) which is related to object size (and profile shape) relative to the local PSF.

Because the PSF shapes vary substantially during the observing period we can test the efficacy of this method directly. Figure 1 shows a plot of mean *corrected* galaxy e_1 and e_2 binned as a function of PSF shape for all the data. One can see that after correction there are residual systematic shape errors for the galaxies, especially where the initial PSF anisotropy is large. This is probably because the correction in Eqn. 4 is exact in the limit of nearly round PSF while much of our data has PSF sufficiently elliptical to require higher order information about the PSF.

Fortunately, for measuring a galaxy-galaxy lensing signal, image quality is less important than for some other types of weak lensing measurements (e.g. cosmic shear). The reason is that one measures tangential shear
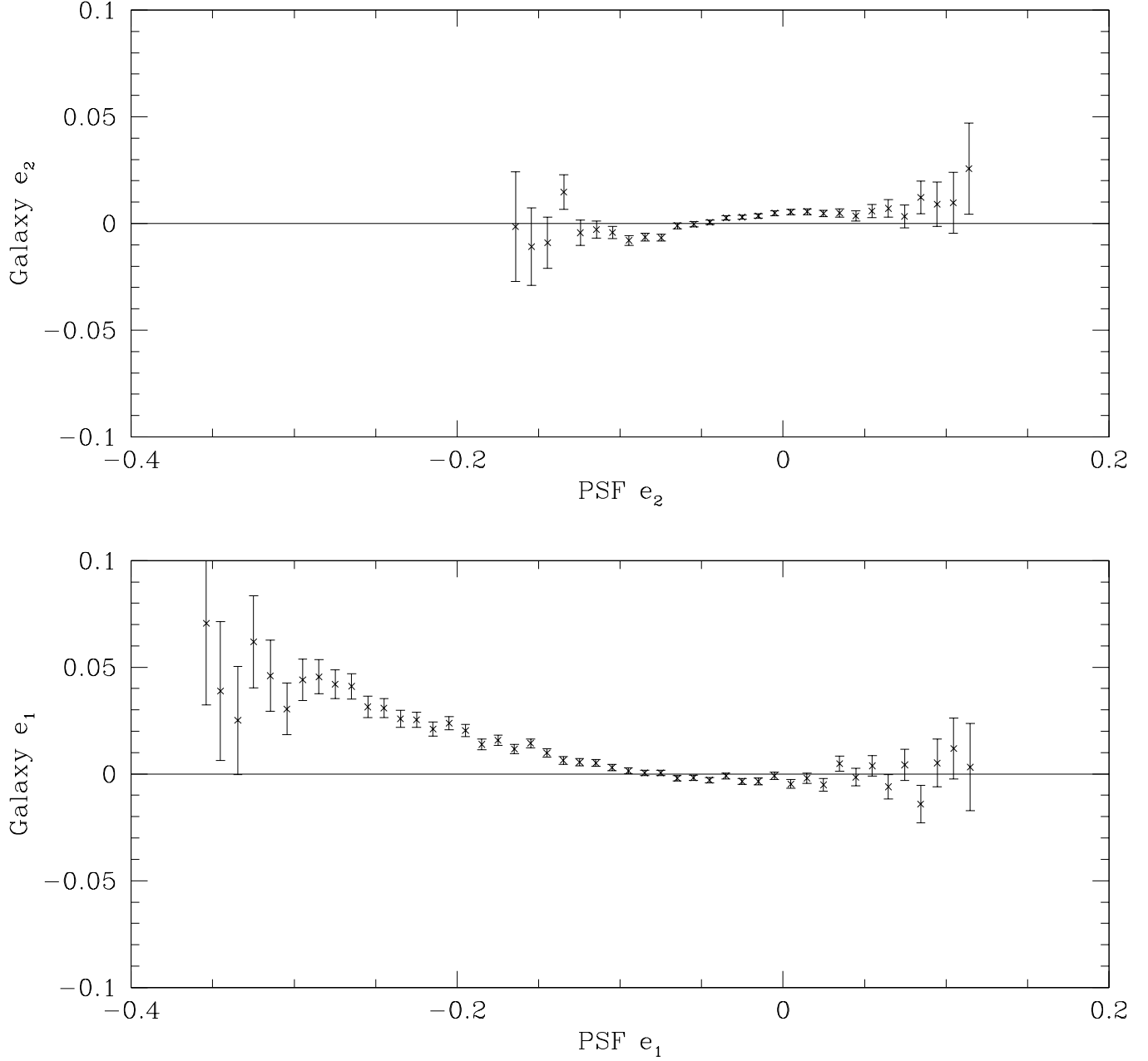
Fig. 1.— Mean *corrected* galaxy shape vs. PSF shape for the r' data. Strong correlations are present indicating imperfect correction for PSF anisotropy.

centered at many different points in the field (see §3.3), hence, most systematics will average out (see §4.3). In order to minimize the effects of systematically biased galaxy shapes we require the foreground galaxies to be surrounded by a radially symmetric distribution of background galaxies. For each foreground galaxy, the centroid of the background galaxy distribution must not be significantly (4σ) different from the position of the foreground galaxy and the distribution itself must have an ellipticity of less than 20% or deviate from circular by less than 3σ (whichever is more). These requirements remove foreground galaxies which are near the edges of the field or near regions that are lacking background galaxies (e.g., because of nearby bright stars or galaxies). By removing such galaxies we reduce potential systematics as each galaxy will have its tangential shear measured in a azimuthally symmetric manner. In addition we fit linear functions to the residual galaxy e_1 and e_2 shown in Figure 1 and subtract the fit from the galaxy shapes.

The PSF will also blur the galaxies resulting in an underestimate of their true ellipticities. This can be corrected by dividing the $e_i(galaxy)$ by $1 - S_{Sm}$. Objects with smear polarizabilities near unity (poorly resolved objects similar in size to the PSF) will have a very large and uncertain correction term. Thus we do not use any galaxies with $S_{Sm} > 0.8$ for our shear measurements. This has the added benefit of eliminating the vast majority of stars which could potentially contaminate our galaxy sample (see §4.2).

When a galaxy image is subject to a shear its shape changes. The ratio of the change in shape to twice the shear is known as the shear polarizability (Kaiser et al. 1995). This is dependent on the shapes of the galaxies and needs to be corrected for when measuring shear. We use the following formula for this correction (Bernstein et al. 2000):

$$S_{Sh} = \frac{\sum_i [w_i(1. - \sigma_{SN}^2 w_i e_T^2)]}{\sum_i w_i}, \tag{5}$$

where the w_i are weights, $w_i = \frac{1}{\sigma_{e,i}^2 + \sigma_{SN}^2}$, $\sigma_{SN} = 0.32$ is the shape noise for galaxies measured from a sample of large, high s/n SDSS images of galaxies, σ_e are seeing-corrected uncertainties (Bernstein et al. 2000), and e_T^2 is the tangential component of the ellipticity. We apply this correction statistically to the final shear measurements (see equation 8) (see §4.2 for details). We note that the galaxy shape uncertainties do not include terms for centroiding error or background misestimation and are therefore slightly underestimated.

3.2. Shear - Theory

Weak gravitational lensing will cause galaxies located behind a mass concentration to appear, on average, tangentially aligned with respect to the center of mass. For gravitational lensing, the relationship between the tangential shear, γ_T, and surface mass density, Σ, is (Miralda-Escudé 1991; Miralda-Escudé 1996),

$$\gamma_T(\theta) = \overline{\kappa}(\le \theta) - \overline{\kappa}(\theta), \tag{6}$$

where $\kappa = \Sigma/\Sigma_{crit}$, the ratio of the surface density to the critical surface density for multiple lensing, and θ is the angular distance from a given point in the mass distribution. The critical surface density depends on the redshift distribution of the background galaxies. The first term on the right is the mean surface density interior to θ and the second term is the mean surface density at θ. In order to measure the tangential shear around angular coordinates (θ_1, θ_2) the distortion of the background galaxies needs to be measured:

$$D_i(\theta_1, \theta_2) = \frac{1}{(1 - S_{Sm,i})} \frac{-(e_{1i}(\theta_{1,i}^2 - \theta_{2,i}^2) + 2e_{2i}\theta_{1,i}\theta_{2,i})}{\theta_{1,i}^2 + \theta_{2,i}^2}, \tag{7}$$

where $\theta_{1,i}$ and $\theta_{2,i}$ are angular distances in R.A. and Dec., respectively, from the foreground galaxy to background galaxy i. The mean tangential shear is:

$$\langle\gamma_T(\theta_1,\theta_2)\rangle = \frac{1}{S_{Sh}}\frac{\sum_i^{N_s} w_i D_i}{2\sum w_i}, \tag{8}$$

where the weights, w_i are described above and N_s is the total number of background galaxies in the region of interest. We do not use any galaxies with seeing-corrected uncertainties of $\sigma_e > 0.64$. The statistical uncertainty in the mean tangential shear, which mostly arises from the intrinsic ellipticity and measurement error of the background galaxies (see §4), is:

$$\sigma^2_{\gamma_T}(\theta_1,\theta_2) = \frac{\sum_i^{N_s} w_i^2 D_i^2}{4S_{Sh}^2(\sum w_i)^2}, \tag{9}$$

where we have assumed that $\langle D\rangle$ is zero, which, in the weak lensing regime, results in a very minor overestimate in σ_{γ_T}.

3.3. Shear - Measurement

The shear from an individual L$_*$ galaxy is predicted to be small (less than 1% for the present data). Therefore we need to average the shear around a large number of foreground galaxies to obtain a statistically significant signal. Ideally one would like to select and scale the foreground galaxies based on their redshifts. However, redshift information is not currently available for the foreground galaxy sample (although the SDSS will eventually measure redshifts for these galaxies) so we choose foreground and background samples based on r' magnitudes. Figure 2 shows plots of measured shear in the g', r', and i' images for $10'' \leq$ radius $\leq 600''$. The lens or "foreground" galaxies have dereddened $16 \leq r^*_0 \leq 18$ and the source or "background" galaxies have $18 \leq r^*_0 \leq 22$ (all magnitudes refer to Petrosian magnitudes, Lupton et al. (2000)). Columns 2, 3 and 4 of Table 1 show the numbers of foreground galaxies, background galaxies and foreground/background pairs, respectively, for each filter. The g' and i' band have fewer galaxies because some of the r'-band selected galaxies are not measurable in those bandpasses. Column 2 of Table 2 shows the mean values of the tangential shear for the radial range 10 - 600$''$.

Our background galaxy sample contains many galaxies which are in front of some of the foreground sample. This can be accounted for if the redshift distributions of the foreground and background galaxies are known. However, there is a complication due to the clustering of galaxies. Some fraction of the background galaxies will actually be galaxies associated with the lensing galaxies and this fraction will decrease as a function of projected distance from the foreground galaxies. If this correction is not made, the shear profile will be radially biased. Figure 3 shows the density of galaxies in the background sample as a function of projected radius from the lens galaxies for the r' data. The g' and i' data are similar. The shear values in Figure 2 have been corrected for this effect by multiplying the measured values by the fractional excess of background galaxies. We assume that there are no coherent distortions in the galaxies associated with the lensing galaxies induced by dynamical interactions.

3.4. Redshifts

In order to convert the shear measurement into mass measurements we need to know three things: 1) the foreground redshift distribution, $n(z_l)$, 2) the background redshift distribution, $n(z_s)$ 3) and the weighting as a
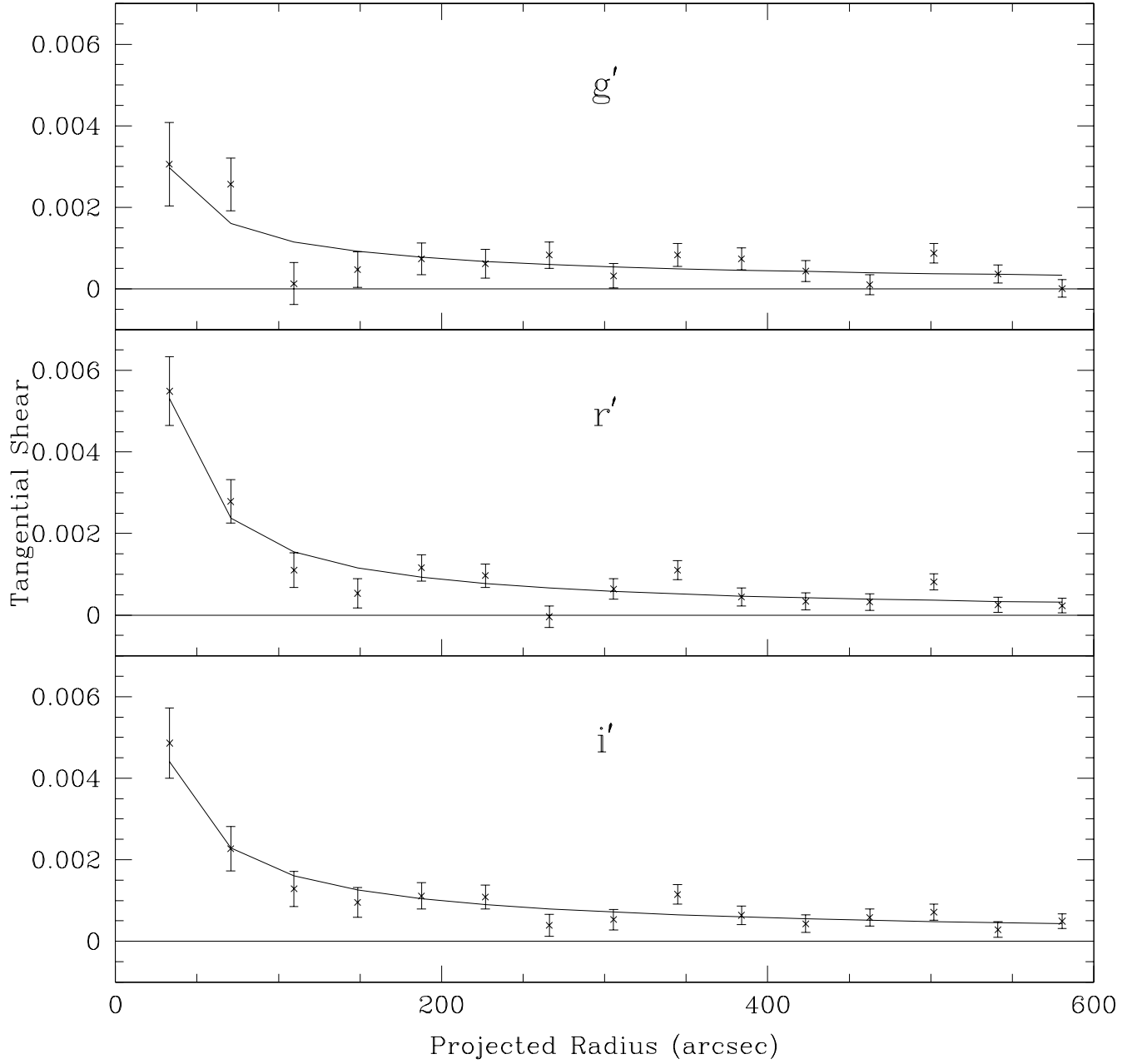
Fig. 2.— Mean shear around foreground galaxies measured from the g, r' and i images (top, middle, bottom). The foreground galaxies have $16 \leq r_0^* \leq 18$ and the background galaxies have $18 \leq r_0^* \leq 22$. See Table 1 for details. The solid lines are the best fit power-law models with parameters given in Table 2. The errorbars are $\pm 1\sigma$
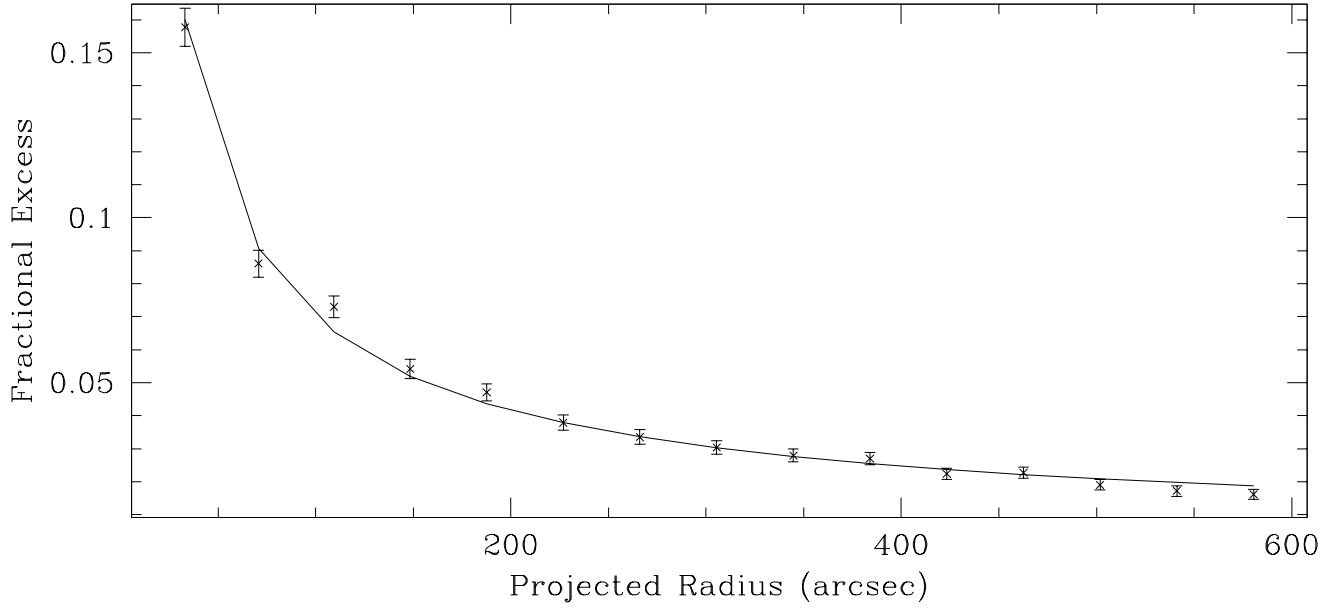
Fig. 3.— Density of "background" galaxies as a function of projected radius from the "foreground" galaxies expressed as a fractional excess. The solid line is a power law with index -0.75. The excess galaxies seen at small radius are most likely associated with the lens galaxies. The diluting influence of these galaxies must be corrected for in the shear measurements. This plot is for r' data, g' and i' are similar. The errorbars represent 1σ Poisson errors.

function of redshift $w(z_s)$. Although the SDSS will eventually measure redshifts for the entire foreground galaxy sample, no spectroscopic redshifts are currently available. Therefore, we use photometric redshifts (photo-z) to estimate the foreground and background galaxy redshift distributions.

The redshift distribution of the SDSS galaxy sample was determined from their u', g', r' and i' photometric data (i.e. photometric-redshifts; Connolly et al. (1995)). Redshifts are estimated using a semi-empirical template fitting technique (Sawicki et al 1997; Connolly et al. 1999). The quadratic difference between the observed galaxy colors and those predicted by a set of model spectral energy distributions are minimized as a function of redshift and galaxy type. This minimization results in an estimated redshift, spectral type and associated uncertainties. The spectral energy distributions used in this analysis are based on the Coleman, Wu and Weedman data set, modified to match the observed colors of the galaxies within the SDSS sample (see Csabai et al. (1999); Budavari et al (1999) for a discussion of these techniques).

To date there exist 1298 galaxies with published spectroscopic redshifts in the equatorial region surveyed by Runs 752 and 756 (identified from the NASA/IPAC Extragalactic Database and the spectroscopic survey of Heyl et al. (1997)). These galaxies extend over the redshift and magnitude intervals of $0 < z < 0.5$ and $r' < 22$ respectively. As such they provide an independent estimate of the systematic and statistical uncertainties in the photometric redshift relation for the SDSS commissioning data. A comparison between the spectroscopic and photometric redshifts shows no systematic offsets in the photometric redshift relation out to $z = 0.5$ (the limit of the spectroscopic data). The dispersion in the photometric redshift relation, at $r = 21$, is $\sigma_z = 0.1$.

Photometric redshifts are currently available for only a portion of our data, and in any case the photometric redshift errors are too large to compute accurate values of Σ_{crit} for each foreground-background galaxy pair. Instead, we compute an expectation value of the quantity of interest $\langle\Sigma_{crit}^{-1}\rangle$, assuming that these galaxies are drawn randomly from the foreground and background redshift distributions, using an $\Omega = 1$ geometry to convert redshifts to physical distances. Specifically, we compute $\langle\Sigma_{crit}^{-1}\rangle$ from the following convolution:

$$\langle\Sigma_{crit}^{-1}\rangle = \frac{1}{N_b N_f} \sum_{i=1}^{N_b} \sum_{j=1}^{N_f} \frac{n_{b,i} n_{f,j}}{\Sigma_{crit,ij}}, \tag{10}$$

where N_b and N_f are the number of foreground and background redshift bins, respectively, n_b and n_f are the number of objects per redshift bin, and $\Sigma_{crit,ij}$ is the critical density corresponding to $z_{f,j}$ and $z_{b,i}$. The values of $\langle\Sigma_{crit}^{-1}\rangle$ for the three filters are given in column 5 of Table 1. Also shown are the mean values (weighted by $\langle\Sigma_{crit}^{-1}\rangle$) of the foreground redshift and angular diameter distance.

4. Sources of Error

4.1. Random Error

The errorbars plotted on the shear profiles in Figure 2 are derived via Equation (9) from the scatter in individual galaxy shape measurements. The two largest contributors to this scatter are the intrinsic ellipticities of the background galaxies (shape noise) with an rms of 0.32, and the error in the shape measurements (e_1, e_2) which is a function of galaxy size and brightness. Improvements in image quality could reduce the second source of scatter in future SDSS data, but the shape noise is an intrinsic property of the galaxy distribution that is independent of image quality. The contributions of both these sources of scatter to uncertainties in the shear decreases as $1/\sqrt{n_b}$, so the factor of $10,000/225 = 44$ increase in sky area in the full SDSS will greatly reduce the statistical uncertainties in the shear measurements.

Another source of scatter arises because the foreground galaxies span a range of redshifts and the shear

measurements are binned by angle. Thus we are averaging over a range of physical radii weighted by $\Sigma_{crit}^{-1}(z_l)$. To estimate how much additional scatter this causes we use the photo-z relationships from §3.4 to estimate n(z). We assume that the galaxies are *identical* singular isothermal spheres and find that at a given projected radius the standard deviation of the shear arising from the lens redshift range is approximately 50% of the mean signal. Given that we have about 28000 foreground galaxies, this translates into an uncertainty of 0.3% and hence is a very small contributor to the uncertainties in Figure 2.

A second source of scatter arises because the foreground galaxies do not have identical masses (we are sampling a range of the galaxy mass function). In order to estimate this we assign an absolute luminosity to each foreground galaxy based on its apparent magnitude (reddening corrected) and photo-z. We then assume that luminosity is proportional to mass squared. This produces a scatter of about 40% in mass which when averaged over all the galaxies produces a similarly small contribution to the shear scatter.

A third source of scatter results from the possible radial asymmetry of the galaxy surface density profiles. The shape of galaxy halos is not well known (and is in fact something that can be measured with weak lensing, although it will require about 10 times more data than we have here) but if we assume that the halo has the same shape as the luminous portion of the galaxy (mean axis ratio of about 0.5) then we can estimate the effect. To do this we assume a pseudo-isothermal elliptical mass distribution (Kassiola & Kovner 1993). We then look at tangential shear in two 90° angular bins, one centered on the major axis and one centered on the minor axis. The ratio of mean shear in the minor axis bin to the major axis bin is 0.55. Therefore, the scatter due to elliptical halos is of similar order to the previous two effects.

We can, therefore, conclude that galaxy shape noise and measurement error are the dominant sources of random uncertainty for our shear measurements.

4.2. Systematic Error

We have already discussed how to correct for one source of systematic error, the dilution of the shear signal due to including galaxies associated with the lenses in the background sample. Additional systematics arise from: inclusion of stars in the background, errors in the correction for blurring by the PSF and errors in the estimate of Σ_{crit}.

Stars will dilute the shear signal by the stellar contamination fraction. Distinguishing between stars and galaxies is difficult at the faint end of our background sample as the two overlap in angular size. We eliminate the vast majority of stars from our background sample by virtue of our smear polarizability cut ($S_{Sm} \leq 0.8$ for inclusion in the background sample). We estimate the residual contamination by making a histogram of S_{sm} for all objects. This has two peaks, a narrow one centered at unity due to stars and a broader one centered at 0.4-0.5 due to galaxies. We use this to estimate that the residual contamination is less than 1%.

Our estimate of Σ_{crit} depends on knowledge of the redshift distribution of the background and foreground galaxies. The error in Σ_{crit} depends on the relative error in the foreground/background redshift distributions and the sensitivity of Σ_{crit} to these errors. We have estimated these distributions based on photometric redshifts. The leading source of error in the mean redshifts is uncertainty in the photometric zeropoints for the commissioning data. Based on comparisons of the photometric redshifts with approximately 500 spectroscopic redshifts the error in the mean is about ± 0.04. This will affect both foreground and background redshifts in a similar manner and thus the effect on the value of Σ_{crit} is small; we conservatively adopt a 95% confidence interval of $\pm 5\%$.

To test our PSF blurring correction we carry out simulations of galaxy fields. The simulated images have noise and seeing characteristics similar to that of the r'-band SDSS images and the simulated galaxies have a similar distribution of sizes. Based on these simulations we conclude that our correction is accurate to 10%.

In conclusion we estimate the 95% confidence limit on systematic errors to be around ±10%.

4.3. Tests

In order to verify the reality of our shear detection we perform several tests. The first test is designed to check if the signal is likely to be due to gravitational lensing and involves rotating the background galaxies by $45°$ and determining if a signal still exists. This is equivalent to calculating the curl of the gradient in κ which should be zero for lensing distortions (Stebbins, Mckay, & Frieman 1996; Luppino & Kaiser 1997). Figure 4 shows the results of this for the three bandpasses with the values given in column 3 of Table 2. The mean "rotated" shear is consistent with zero for all three cases.

The second test is designed to check for systematics in the background galaxy shapes and involves measuring shear around random points using the same background galaxies as were used for the original shear measurement. Figure 5 shows a plot of the mean shear around 1000 sets of random points for each bandpass. Each set contains as many points as the number of foreground galaxies. The maximum absolute value for any of the radial points from these simulations is less than 20% of the corresponding errorbar in the observed shear around the galaxies and the mean is 7%. Even though we are using many more random points than there are foreground galaxies the errorbars do not continue to decrease as we are greatly oversampling the region. Thus it is not possible to tell if this systematic is significant. Therefore, in the following analysis, where appropriate, we quote results with and without the systematics subtracted from our measured shear. In all cases, including the systematic does not substantially change the result.

The third test is designed to check if the measured background galaxy shapes are being biased by the faint tails of the foreground galaxies' surface brightness distributions. For this test we measure shear around 26397 bright stars (Figure 6) and find $\langle \gamma_T \rangle = -3.6 \pm 5.5 \times 10^{-5}$, consistent with zero. Therefore, it is unlikely that gradients in the sky background are resulting in significant systematic errors in the galaxy shapes.

Based on the low level of possible systematic errors inferred from these three tests we conclude that our shear measurement is real, results from gravitational lensing and is not due to PSF systematics or measurement error.

5. Modeling

5.1. Galaxy-Shear Correlation Function

The galaxy-galaxy shear signal is a direct measure of the galaxy-mass correlation function (Figure 2). We fit power-law models of the form:

$$\gamma_T(\theta) = \gamma_{T0} \left(\frac{1'}{\theta} \right)^{\eta}, \tag{11}$$

to each of the shear profiles where θ is the angular radius. The best fit values are shown in Table 2 and the confidence intervals are shown in Figure 7. The 95% confidence range for the slope from the three bandpasses combined (using the full error covariance matrix) is $\eta = 0.7 - 1.1$. A shear profile well-fit by a power-law implies the same power-law form for the surface mass density profile.

As the SDSS obtains more imaging data, we will be able to push this measurement out to larger radii. It will then be interesting to compare this number to the galaxy-galaxy correlation function (two-point correlation function) for a direct measurement of the bias.
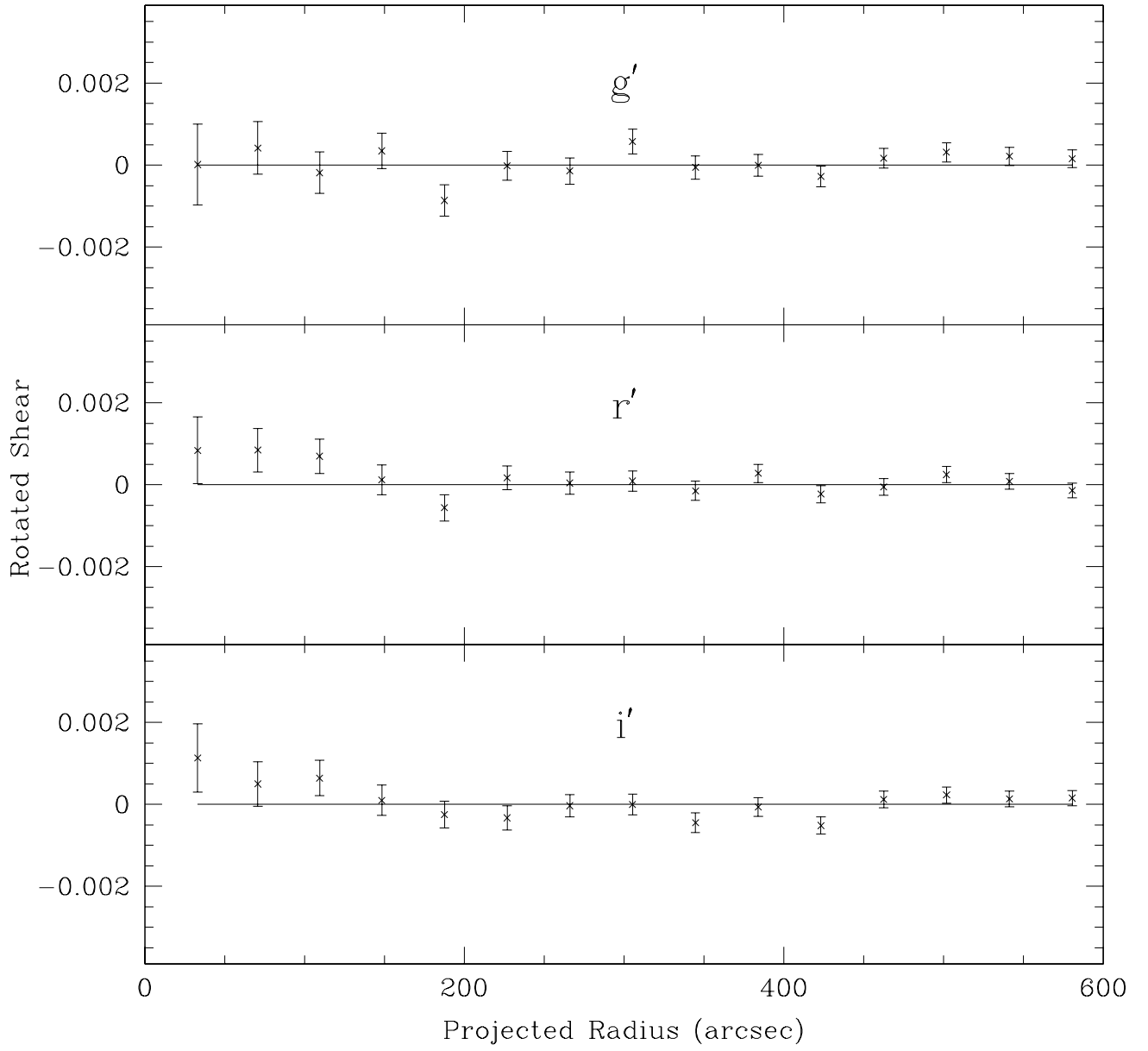
Fig. 4.— As in Fig. 2 but now the background galaxies have been rotated by 45°. The signal is consistent with zero for all three bandpasses. The errorbars are $\pm 1\sigma$
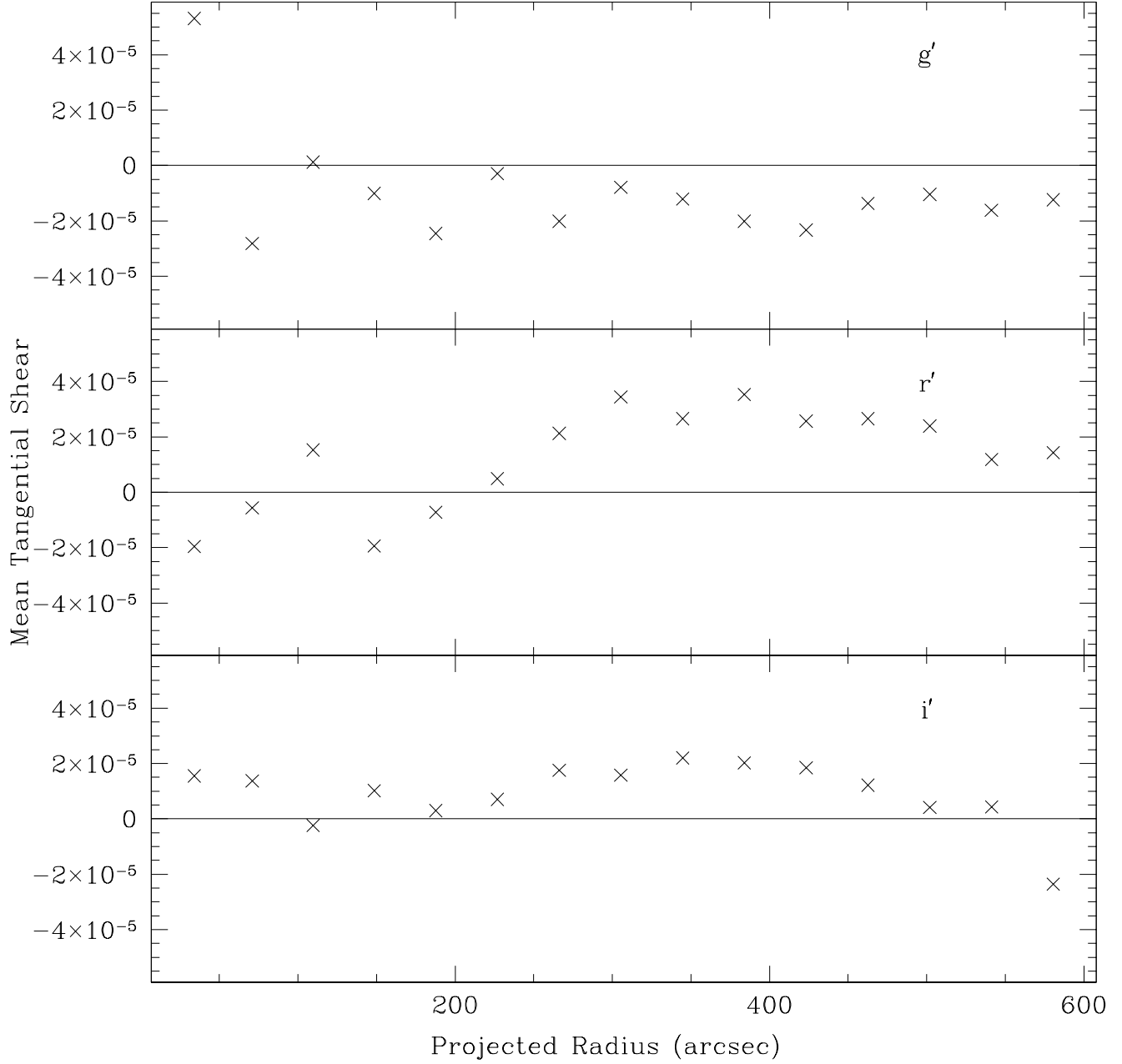
Fig. 5.— Mean shear around random points measured using the same background galaxies as Figure 2. The total random points are 1000 times the number of true foreground galaxies. In the absence of systematics the values should be zero. There is some evidence for systematics in each bandpass. Note, the 'Tangential Shear' axis has a range that is 1.5% of the other shear plots.
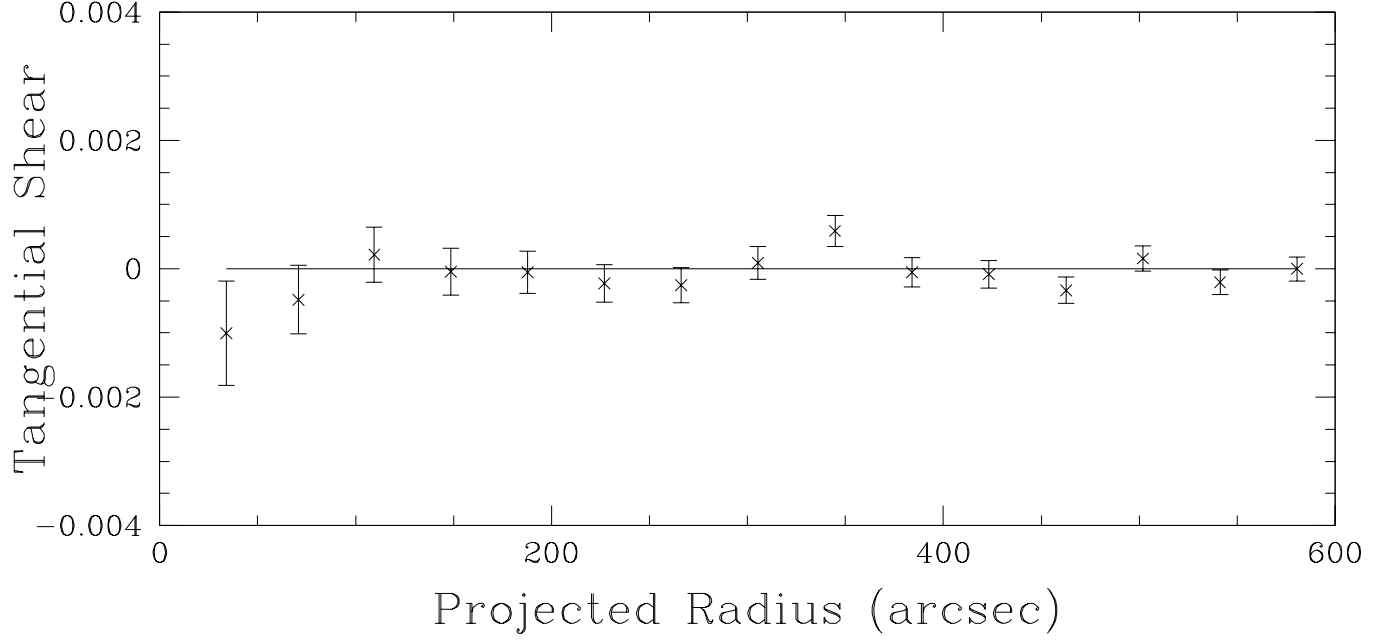
Fig. 6.— Mean shear around 26397 bright stars (r'-band). The signal is consistent with zero implying that measurements biases due to gradients in the surface brightness are not important. The errorbars are $\pm 1\sigma$
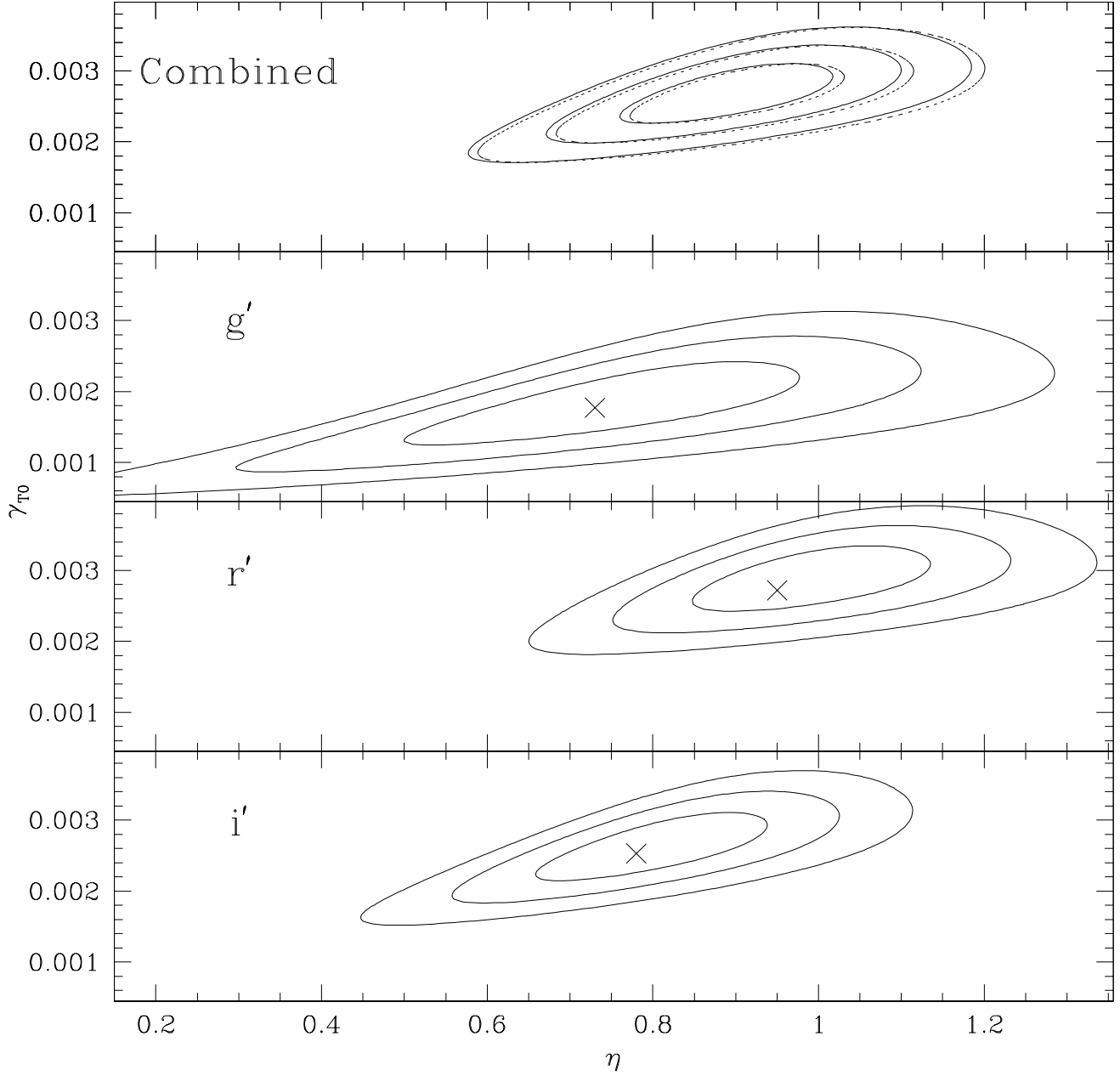
Fig. 7.— One, two and three σ confidence intervals for the parameters γ_{T0} and η for the i', r', and g' filters (bottom to second from top) and the combined data (top) (see Equation 11). The dashed contours in the top panel show the confidence ranges if the systematic errors shown in Figure 5 are subtracted from the shear measurements prior to fitting.

5.2. Galaxy Parameters

It is possible to constrain interesting galaxy parameters from these shear measurements, however, this is complicated by the clustering of galaxies. Because galaxies are correlated in space the measured shear profiles have contributions from the central galaxies and neighboring galaxies. As one goes to larger projected radii, the fractional contribution of the neighboring galaxies increases. To correctly infer the mean characteristics of the central galaxies this correlation must be taken into account. Figure 8 shows the excess number density centered on foreground galaxies (foreground galaxy autocorrelation function). The excess number density is well fit by a function of the form:

$$\phi(\theta) = 0.62 \left(\frac{1''}{\theta}\right)^{0.72} \mathrm{arcmin}^{-2}. \tag{12}$$

Also shown in Figure 8 is the cumulative number of neighboring galaxies based on integrating the fit. Methods of dealing with the neighboring galaxies have been discussed in Brainerd et al. (1996); Schneider & Rix (1997); Hudson, Gwyn, Dahle & Kaiser (1998). These approaches involve parameterizing the galaxy surface mass distributions and the use of scaling relationships to account for variation in the lens galaxies. Maximum likelihood is used to determine the most probable values of the galaxy parameters. These approaches work best when there is at least crude redshift information available. Lacking such information, we adopt a different and somewhat simpler approach to modeling the shear.

The first contribution to the tangential shear is due to the central galaxy. Similar to Brainerd et al. (1996) and Schneider & Rix (1997) we approximate the mass density of the lensing galaxies as a truncated isothermal:

$$\rho(R) = \frac{\sigma_v^2 s^2}{\pi G R^2 (R^2 + s^2)} \tag{13}$$

where σ_v is the line-of-sight velocity dispersion for $r << s$, and s is the characteristic outer scale. For $R << s$ this mass distribution produces a near flat rotation curve as seen in observations of disk galaxies. For $R >> s$ the profile falls as $1/R^4$ and the shear falls off very rapidly. The corresponding surface density profile is:

$$\Sigma_g(\theta) = \frac{\sigma_v^2}{2G\theta} \left(1 - \frac{\theta}{\sqrt{\theta^2 + s^2}}\right), \tag{14}$$

The second contribution is due to the neighboring galaxies. We assume that all the galaxies have identical mass profiles given by equation (14) and that there is no contribution to the shear from galaxies not in our foreground sample. The mass density profile resulting from the neighboring galaxies is given by the convolution between the number density and the galaxy surface density.

$$\Sigma_{tot}(\theta) = \left[\Sigma(\theta') * \phi(\theta')\right](\theta). \tag{15}$$

and the shear is given by equation 6.

We carry out this convolution numerically and use least-squares fitting to the data shown in Figure 2 to derive the best fit values for σ_v and s (columns 7 and 8 of Table 2). The values for σ_v assume the $< D_l >$ shown in Table 1. The fits are shown in Figure 9. In the inner regions the shear is completely dominated by the central galaxy but the neighboring galaxies contribute roughly half the shear at $600''$. Figure 10 shows the 1, 2, and 3σ confidence regions for the fits to velocity dispersion and s for the three bandpasses and to the
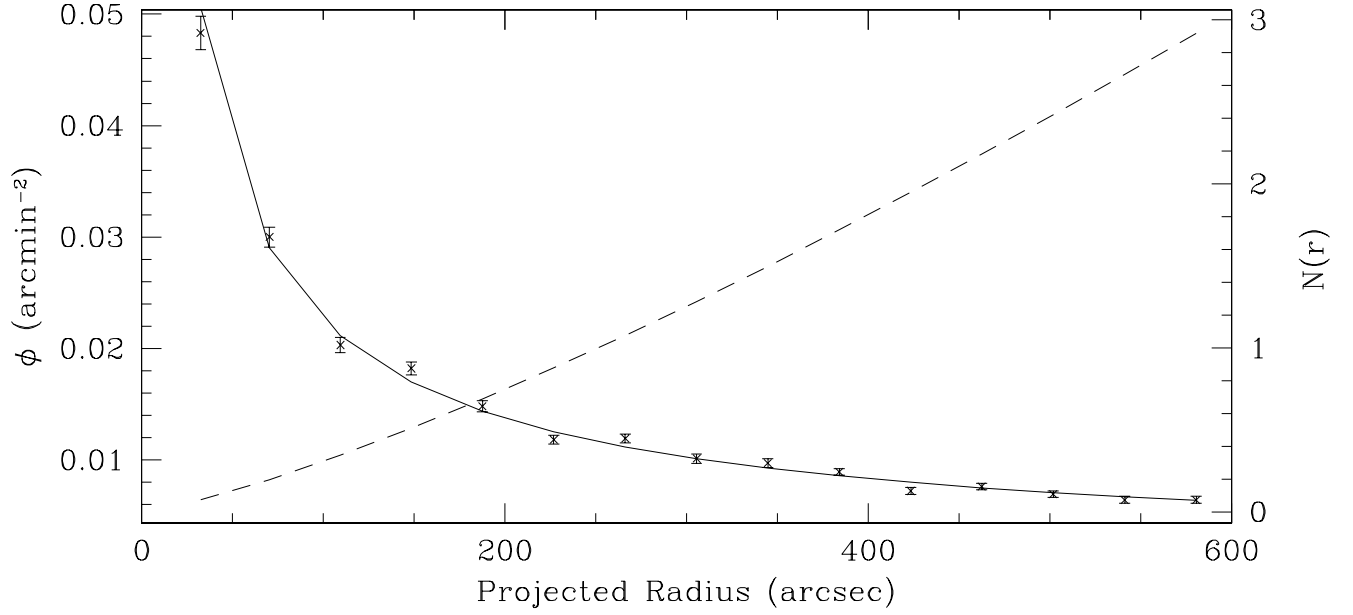
Fig. 8.— Density (points) and cumulative number (dashed line) of excess "foreground" galaxies as a function of projected radius from the central galaxy. The solid line is a power-law with index -0.72. Both of these exclude the central galaxy. These neighboring galaxies will contribute to the shear signal.
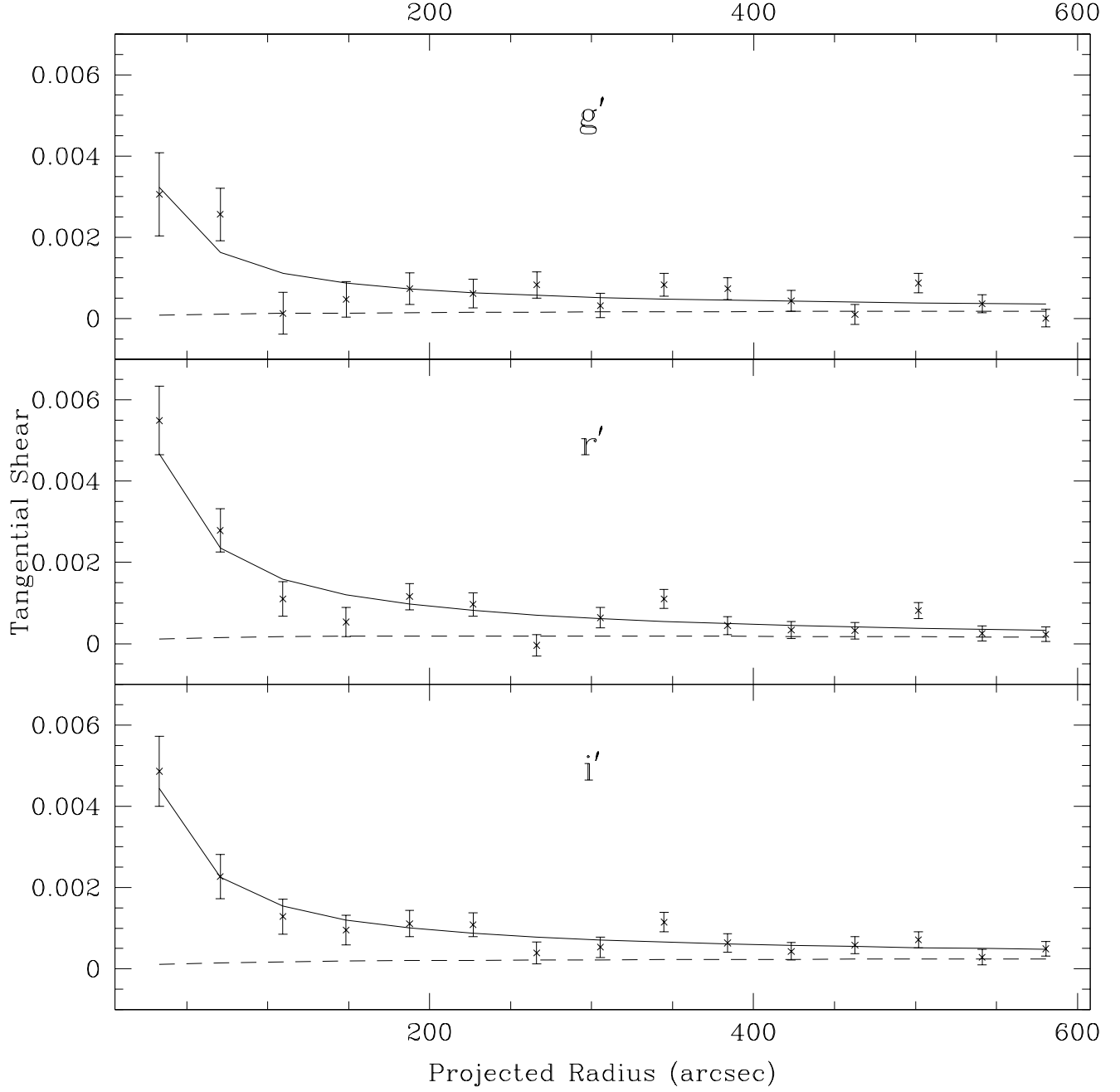
Fig. 9.— Shear around foreground galaxies as in Figure 2. The solid lines are the estimated shears due to the central and neighboring galaxies. The dashed lines are the shears due to the neighboring galaxies exclusively.

combined data set (using the full error covariance matrix). Also shown are the confidence regions for the fits to the shears which have had the systematics shown in Figure 5 subtracted. The differences are very small.

There are three important conclusions. The first is that the velocity dispersion is well constrained (at least for $s \leq 900''$) and is in the range 150-190 km s^{-1} (95% confidence, 145-195 km s^{-1} if one includes systematics). The second is that the minimum value for s is well constrained to be greater than 140'' (95% confidence) which is about 260 h^{-1} kpc. The third conclusion is that the upper limit on s is completely unconstrained with the present data. The reason for this is that large changes in s mainly affect the large radii points and even substantial fractional changes in the shear at large radii only change χ^2 by a small amount.

One of the shortcomings of our analysis is that we do not account for the shear contribution of neighboring galaxies fainter than our foreground sample (Figure 3). If these galaxies contain a substantial fraction of the mass then the consequence of ignoring these galaxies is to overestimate both the outer scale radius and the velocity dispersion. Alternatively, one could interpret these galaxies as actually being a constituent of the central galaxies and then the inferred parameters (σ_v and s) will include their mass contribution. We will consider their contribution in detail in a future paper once we have spectroscopic and photometric redshifts and greater field coverage.

5.3. Galaxy-Mass Correlations

Another way of looking at the tangential shear measurements is in terms of 2-point correlation functions. The galaxy angular auto-correlation function, $w_{\rm gg}(\theta)$, has been extensively studied, and the $\gamma_T(\theta)$ that we measure may be interpreted as the galaxy-shear correlation function, which can be related to the spatial galaxy-mass correlation function, $\xi_{\rm gm}(r)$ (see Kaiser (1992)). Since the measured $\gamma_T(\theta)$ is well fit by a power law in angle the inferred galaxy-mass correlation will also be well fit by a power law in separation, i.e.

$$\xi_{\rm gm}(r) = \left(\frac{r_{\rm gm}}{r}\right)^{\gamma} \tag{16}$$

where $\gamma = \eta + 1$, and η is as given in Table 2. For the purpose of this analysis we assume a universal non-evolving correlation function. Of course different types of galaxies are known to have different clustering properties and our foreground galaxy sample is not homogeneous, containing more dim galaxies nearby and only luminous galaxies far away. The inferred value of $\gamma \approx 2$ is consistent with the clustering of galaxies on the sub-Mpc scale we are probing, as is indicated by the slope of the excess counts shown in Figure 8, which implies a galaxy auto-correlation function

$$\xi_{\rm gg}(r) \approx \left(\frac{r_{\rm gg}}{r}\right)^{1.72}. \tag{17}$$

Thus a model where the galaxies trace the mass with a scale-independent bias is consistent with our measurements.

To interpret the amplitude, and not just the slope, one must have knowledge of the redshift distribution of the galaxies, both foreground and background. As we have mentioned this is somewhat uncertain, but we proceed in this section using a model redshift distribution of background and foreground galaxies based on the models of Koo, Gronwall, & Bruzual (1993). Using the Limber equation for $\gamma_T(\theta)$ (see Kaiser (1992)) and imposing a power law model with slope $\gamma = 1.72$, taken from the excess counts, we infer for the correlation length of the mass-galaxy cross-correlation

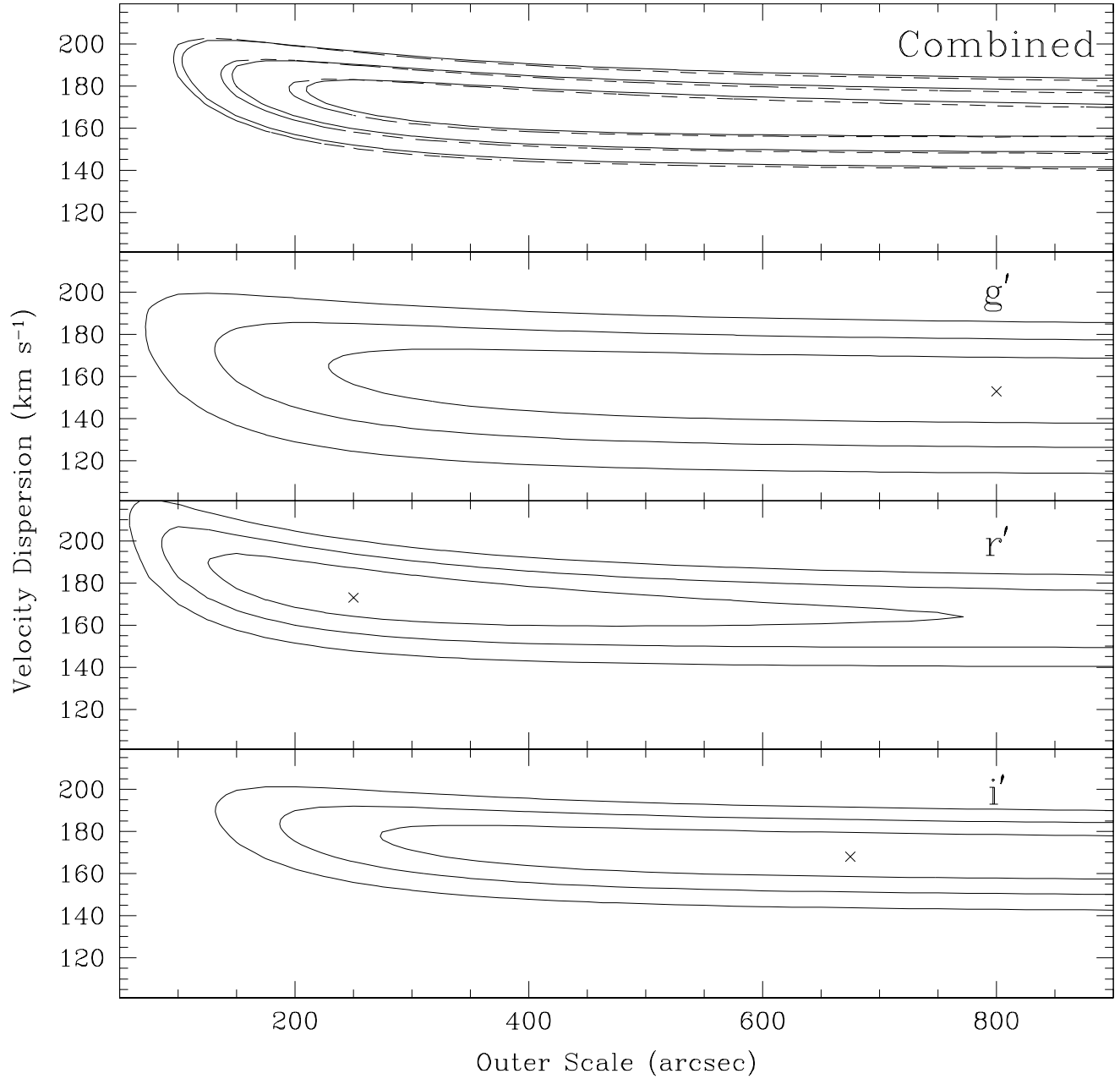$$r_{\rm gm} \sim 3h^{-1}\Omega_{\rm m,0}^{-0.57}{\rm Mpc}. \tag{18}$$

Fig. 10.— One, two and three σ confidence regions for velocity dispersion and s, the outer scale for i', r', and g' (bottom to second from top) and for the combined data set (top). The points mark the best fit values. The dashed contours in the top panel show the confidence ranges if the systematic errors shown in Figure 5 are subtracted from the shear measurements prior to fitting.

where $\Omega_{m,0}$ is the density of clustering (mostly dark) matter in units of the critical density. Since we are mostly probing the mass-galaxy correlations on sub-Mpc scales this inference involves an extrapolation of nearly an order of magnitude in separation, and since the actual slope, η, is not tightly constrained by our measurements this extrapolation is highly uncertain. This uncertainty combined with the uncertainties in the actual redshift distribution means that this value for r_{gm} should be interpreted with great caution, and is mostly meant to put our results into a familiar context. The fact that it is close to the correlation length of galaxy clustering, $r_{gg} \approx 5h^{-1}\mathrm{Mpc}$, is encouraging, although hardly surprising since have obtained reasonable results for galaxy mass profiles.

Another approach is to compare $\gamma_T(\theta)$ with the galaxy clustering implied by the excess counts of Figure 8 (see van Waerbeke (1998) for a similar type of analysis). The measurement error for the counts is much smaller than for the shear, so we again assume the slope, $\gamma = 1.72$, implied by the excess counts. We relate the mass-galaxy cross-correlation function to the galaxy auto-correlation function by

$$\xi_{\mathrm{gm}}(r) = \frac{R}{b}\xi_{\mathrm{gg}}(r) \tag{19}$$

where R and b are assumed independent of separation. The bias factor, b, is traditionally defined by the ratio of the rms inhomogeneities in galaxies and in mass i.e. for scale-dependent bias $b = \sqrt{\xi_{\mathrm{gg}}(r)/\xi_{\mathrm{mm}}(r)}$; but here we measure the cross-correlation and this may require an additional parameter, R (Dekel & Lahav (1999); Pen (1998)). By definition $R \in [-1, 1]$, and for linear bias $R = 1$. Without going into details the measured ratio of $\gamma_T(\theta)$ to the excess counts tells us that

$$\Omega_{\mathrm{m},0}\frac{R}{b} \approx 0.3 \tag{20}$$

on the sub-Mpc scale. The fact that $\Omega_{\mathrm{m},0}$ with exponent 1 (approximately) appears in this equation rather than with a smaller exponent is a consequence of the very small redshifts of the galaxies we are using. Although this result does not require the large extrapolation needed to infer r_{gm}, we are still making assumptions about the redshift distributions and the slope, so this result is only meant to be suggestive. A more quantitative analysis with less restrictive assumptions and going to larger physical scales will follow, using more data, better redshift determinations, and a proper analysis of $w_{\mathrm{gg}}(\theta)$. Our preliminary result is consistent with currently fashionable cosmological models with low $\Omega_{\mathrm{m},0}$ and moderate b, but using our measurements we cannot disentangle the relative contribution of the three parameters, $\Omega_{\mathrm{m},0}$, b and R. In the future lensing studies of SDSS data may be able to measure the shear-shear correlations at low redshifts which would allow us to determine $\Omega_{\mathrm{m},0}/b^2$, and studies of the strength of lensing with redshift may be able to disentangle $\Omega_{\mathrm{m},0}$ from R/b, just using lensing from SDSS.

6.   Discussion

Our value for the velocity dispersion is consistent with the galaxy-galaxy lensing measurements of Brainerd et al. (1996) ($\sigma_v = 155 \pm 55$ km s^{-1}), Dell'Antonio & Tyson (1996) ($\sigma_v = 185^{+30}_{-35}$ km s^{-1}), and Hudson, Gwyn, Dahle & Kaiser (1998) ($\sigma_v = 150 \pm 30$ km s^{-1}) (all uncertainties are $\pm 1\sigma$). All three of these studies used lens galaxies at much higher redshifts than considered here (particularly the last two which utilize the Hubble Deep Field (Williams et al. 1996) and had mean lens redshift of around 0.6) and were measuring shear at much smaller radii than considered here.

The 95% confidence lower limit on the outer scale radius (260 h^{-1} kpc) implies that there is a great deal of mass at large radius in galaxies. In Figure 11 we plot a cumulative mass distribution for $\sigma_v = 170$ km s^{-1}and

$s = 140''$. Even for this minimum mass case we find M(r)$\approx 5 \times 10^{12} h^{-1}$ M$_\odot$ for $r = 600''$. The mean mass profile is averaged over galaxies spanning a wide range of environments, varying from low density regions to dense cluster centers. Therefore, what exactly do the inferred galaxy parameters mean? For example if, as indicated by some recent observations, clusters have large mass components which are not associated with individual galaxies (Tyson, Kochanski & Dell'Antonio 1998) this mass will be included in our shear measurements. The galaxy-galaxy shear signal is a measure of all the mass correlated with galaxy positions (even if the mass is not gravitationally bound to the galaxies). The inferred mean profile is, therefore, based on a fit to all the mass, both bound and unbound, which is correlated with the galaxy positions and is a measure of the mean mass per galaxy over a representative sample of the universe. We note that if there is a large mass component in the universe which is not correlated with galaxy positions then our procedure underestimates the mass per galaxy. Zaritsky & White (1994) measured the mass within $150 h^{-1}$ kpc for a sample of isolated disk galaxies with rotation velocities near 250km s^{-1} obtaining M $= 1.1 - 2.0 h^{-1} \times 10^{12}$ M$_\odot$ (90% confidence). The upper limit is similar to the value plotted in Figure 11 although direct comparison is dubious given the different ways the galaxies were selected. Both results, however, imply a large extent to the halo.

An important value is the ratio of galaxy mass to light (M/L) as one can use it to estimate the density parameter $\Omega_{galaxies}$. The SDSS photometric pipeline yields galaxy photometry within the Petrosian radius (Lupton et al. 2000) which have a mean value of $5''$ for the data used here. Using the photo-z measurements described in §3.4 we find $\langle L(\theta < 5'') \rangle = 8.7 \pm 0.7 \times 10^9 h^{-2}$ L$_{g'\odot}$, $1.4 \pm 0.12 \times 10^{10} h^{-2}$ L$_{r'\odot}$, $1.8 \pm 0.14 \times 10^{10} h^{-2}$ L$_{i'\odot}$. Figure 11 shows the cumulative mass-to-light profile for the minimal galaxy ($s = 140''$) assuming all the galaxy light is contained within $5''$. Also shown is the cumulative M/L profile where we have extrapolated the light profile by assuming it is an exponential with scale length similar to that of the Milky Way (5 kpc Gilmore et al. (1990)). Values of M$_\odot = 5.06, 4.64, 4.53$ (Fukugita et al. 1999) for g', r', and i', respectively, have been used. The region within $100 h^{-1}$ kpc has M/L$'_r \approx 50 h$ M$_\odot$/L$_{r',\odot}$ and for the largest radii measured ($\sim 1 h^{-1}$ Mpc) it rises to a value similar to what is seen in clusters. These results are similar with the observed dependence of M/L on scale obtained by Bahcall et al. (1995) using observations of galaxies, groups and clusters. For higher values of s the M/L is correspondingly higher, particularly at large radii. Note that we have not made k or evolution corrections and include only light associated with galaxies (e.g., we do not include possible contributions from intracluster light).

7. Conclusions and Future Work

In this paper we have presented the first weak lensing results from the Sloan Digital Sky Survey. One of our most important conclusions is that weak lensing studies are possible with the SDSS despite the fact that it is a relatively shallow drift-scan survey. The data analyzed here are 225 square degrees of early commissioning images which suffered from poor image quality. Despite this we detect a galaxy-galaxy lensing signal around a large sample of foreground galaxies in three bandpasses (g', r' and i') at very high significance.

We present power-law fits to the shear signal and find slope values ranging from 0.7-1.1 (95% confidence range). Our attempts to determine galaxy parameters yielded a galaxy velocity dispersion of $\sigma_v = 150 - 190$ km s^{-1}(95% - 145 - 195 km s^{-1}including systematics) and a 95% lower limit of $140''$ ($260 \ h^{-1}$ kpc) for the outer scale radius. It should be noted that these parameters may include significant contributions from inter-galactic mass provided this mass is correlated with galaxy positions. This lower limit on s leads to a value of M/L$'_r \geq 200 h$ M$_\odot$/L$_{r',\odot}$ within a projected radius of $1 \ h^{-1}$ Mpc.

While our results can be used to constrain the profile and velocity dispersion of galactic halos, at large scales it is more meaningful to use them as a measure of the projected galaxy-mass correlation function. The dividing line between galactic halos and large-scale structure is somewhat arbitrary, but a rough guide is provided by the fact that galactic halos cannot exist as virialized structures on scales much larger than $100 \ h^{-1}$ kpc, since the dynamical time becomes larger than the age of the universe. We present a preliminary determination of
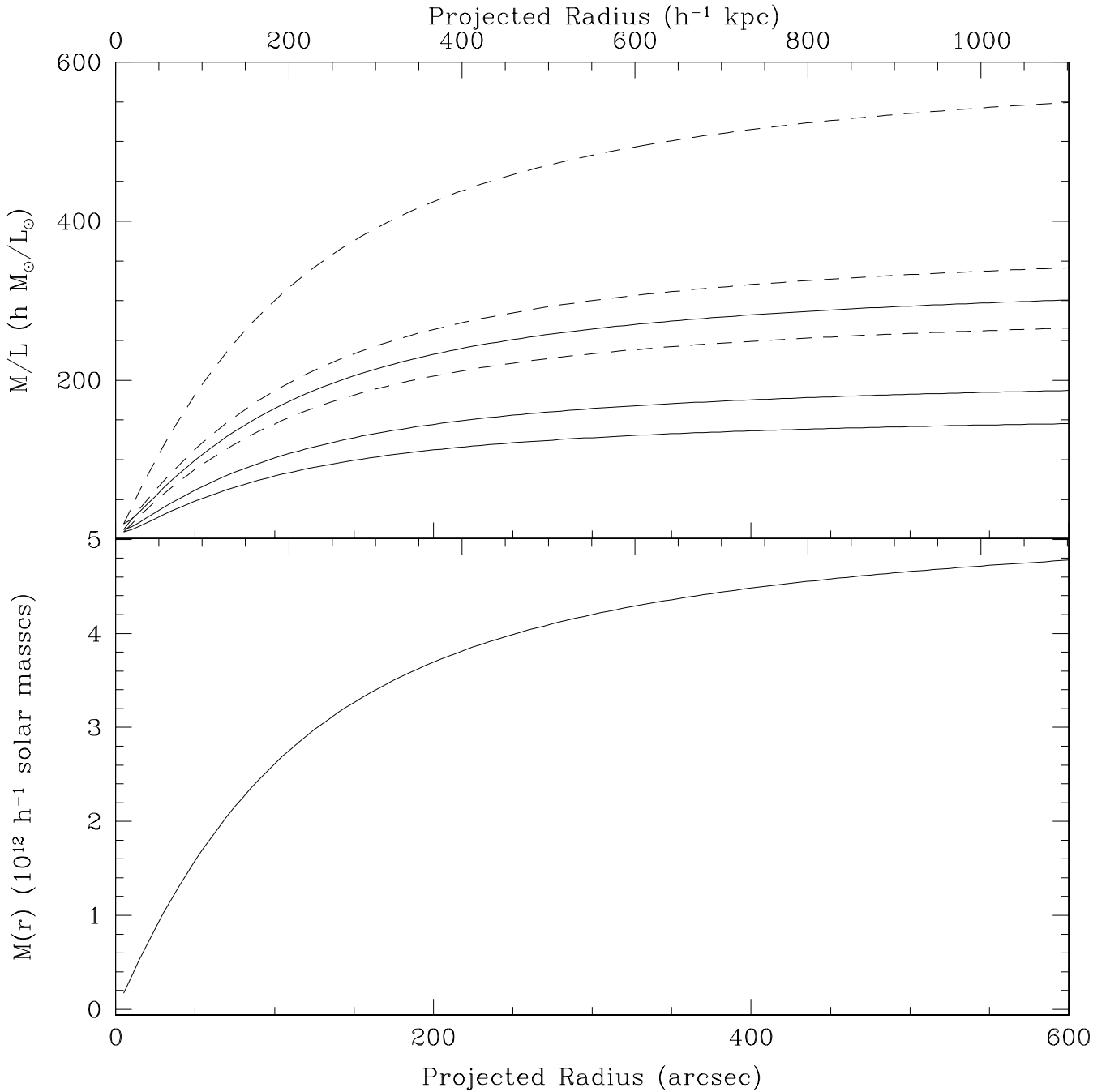
Fig. 11.— Cumulative mass (lower) and mass-to-light profiles (upper) for $\sigma_v = 170$ km s^{-1} and $s = 140''$. The dashed M/L profiles assume all the galaxy light is within $5''$ of the center (as measured) while the solid lines extrapolate the light profile as described in the text. The profiles are g', r', i' from top to bottom. This represents the minimal mass model (95% lower limit on s) so the true profiles are likely to have higher values.

the galaxy-mass correlation function finding a correlation length similar to the galaxy autocorrelation function and consistency with a low matter density universe with modest bias. However, degeneracies between Ω and bias complicate the interpretation.

It will be useful to compare our future results on larger scales with theoretical models of the galaxy-mass correlation. The lensing strength depends on the amplitude of fluctuations in the absolute mass density associated with galaxies. Therefore by comparing with theoretical predictions, or through a direct inversion of the data, we will be able to constrain the biasing of galaxies, the mean density parameter Ω, and the dark matter power spectrum. The accuracy with which these parameters can be independently constrained will be aided by the increased sample size, redshift information, and combination with other measures such as the angular clustering of galaxies and probes of field lensing. We will explore these approaches in future work by using simulated mock catalogs as well as analytical models of halo-mass correlations (McClelland & Silk 1977; Sheth & Jain 1997).

Ongoing improvements in the SDSS data will greatly enhance galaxy-galaxy lensing studies. First, the image quality should improve as the telescope optics are designed to yield PSFs with ellipticities of less than 12%. Second, we will have detailed spectra for all foreground galaxies and photometric redshifts for a large fraction of our background sample. This will allow us to put all the foreground galaxies on the same physical scale and will greatly improve our ability to interpret the galaxy-galaxy lensing measurement in terms of galaxy parameters. The third is that the coverage will increase by a factor of fifty over what we have presented here, which, if our uncertainties remain dominated by random errors, implies a signal-to-noise improvement by a factor of seven.

Finally, if the SDSS achieves its imaging design goals, other types of weak lensing studies will also be possible (Gould & Villumsen 1994; Stebbins, Mckay, & Frieman 1996). These include the search for mass overdensities and measurement of the cosmic shear. Of particular interest is the 250 square degree Southern survey, where repeat scans will produce images two magnitudes fainter than the main survey.

REFERENCES

Bahcall, N. A., Lubin, L. M. & Dorman, V. 1995, ApJ, 447, L81

Bernstein, G. M., Smith, D., Jarvis, M. & Fischer, P. 1999, in preparation.

Brainerd, T. G., Blandford, R. D., & Smail, I. 1996, ApJ, 466, 623.

Budavári, T., Szalay, A.S., Connolly, A.J., Csabai, I. & Dickinson, M.E., 1999, in preparation

Connolly, A.J., Csabai, I., Szalay, A.S., Koo, D.C., Kron, R.G. & Munn, J.A., 1995, AJ, 110, 2655

Connolly, A.J., Budavári, T., Szalay, A.S. & Csabai, I., 1999, to appear in "Photometric Redshifts and High Redshift Galaxies", eds. R. Weymann, L. Storrie-Lombardi, M. Sawicki & R. Brunner, (San Francisco: ASP Conference Series)

Csabai, I., Connolly, A.J., Szalay, A.S. & Budavári, T., 1999, AJ, submitted

Coleman, G.D., Wu., C.-C. & Weedman, D.W., 1980, ApJS, 43, 393.

Dekel, A., & Lahav, O. 1999, ApJ, 520, 24.

Dell'Antonio, I. P. & Tyson, J. A. 1996, ApJ, 473, L17

Doi, M. et al. 2000, in preparation

Fan, Xiaohui, et al. 1999, AJ, 118, 1

Fukugita, M., Ichikawa, T., Gunn, J. E., Doi, M., Shimasaku, K., & Schneider, D. P. 1996, AJ, 111, 1748.

Fukugita, M., Ichikawa, T. & Sekiguchi, M. 1999, in preparation.

Gould, A. & Villumsen, J. 1994, ApJ, 428, L45.

Gilmore, G., King, I. R. & van der Kruit, P. 1990, "The Milky Way as a Galaxy", University Science Books, Mill Valley California.

Griffiths, R. E., Casertano, S., Im, M. & Ratnatunga, K. U. 1996, MNRAS, 282, 1159

Gunn, J., et al., 1998, AJ, 116, 3040.

Heyl, J., Colless, M., Ellis, R.S. & Broadhurst, T., 1997, MNRAS, 285, 613

Hudson, M. J., Gwyn, S. D. J., Dahle, H. & Kaiser, N. 1998, ApJ, 503, 531.

Kaiser, N. 1992, ApJ, 388, 272.

Kaiser, N., Squires, G. & Broadhurst, T. 1995, ApJ, 449, 460.

Kassiola, A, & Kovner, I. 1993, ApJ, 417, 450.

Kent, S. M. et al. 2000, in preparation.

Koo, D.C., Gronwall, C., Bruzual, G.A. 1993, ApJ, 415, 272.

Luppino, G. A. & Kaiser, N. 1997, ApJ, 475, 20

Lupton, R. H. et al 2000, in preparation.

McClelland J., Silk J., 1977, ApJ, 217, 331

Mellier, Y. 1999, ARAA, Vol. 37.

Miralda-Escudé, J. 1991, ApJ, 370, 1.

Miralda-Escudé, J. 1996, in "IAU 173: Astrophysical Applications of Gravitational Lensing", eds. C. S. Kochanek & J. N. Hewitt, (Kluwer), p. 131.

Pen, U. 1998, ApJ, 504, 601.

Petravick, D. et al. 2000, in preparation.

Pier, J. R. et al. 2000, in preparation.

Sawicki, M.J., Lin, H. & Yee, H.K.C., 1997, AJ, 113, 1

Schlegel, D. J., Finkbeiner, D. P., & Davis, M. 1998, ApJ, 500, 525.

Schneider, P. & Rix, H. 1997, ApJ, 474, 25.

Sheth, R. & Jain, B. 1997, MNRAS, 285, 231.

Siegmund et al. 2000, in preparation.

Stebbins, A., Mckay, T., & Frieman, J. 1996, in "IAU 173: Astrophysical Applications of Gravitational Lensing", eds. C. S. Kochanek & J. N. Hewitt, (Kluwer), p. 75.

Tucker, D. L. et al. 2000, in preparation.

Tyson, J. A., Valdes, F., Jarvis, J. F., Mills, A. P., JR. 1984, ApJ, 281, L59.

Tyson, J. A. , Kochanski, G. P. & Dell'Antonio, I. P. 1998, ApJ, 498, L107

Uomoto, A. et al. 2000, in preparation

van Waerbeke, L. 1998, A&A, 334, 1.

Williams et al. 1996, AJ, 112, 1335.

Zaritsky, D. & White, S. D. M. 1994, ApJ, 435, 599.

Table 1.   Data

Filter	Foreground	Background	Pairs	$< \Sigma_{crit}^{-1} >$ $\mathrm{g}^{-1}\ \mathrm{cm}^2$	$< z_l >$	$< D_l > H_0/c$
g'	28134	1213862	13471567	0.343	0.168	0.123
r'	27890	1552721	16913287	0.392	0.172	0.126
i'	27945	1447336	15809470	0.403	0.173	0.126

Table 2.   Model Fits

Filter	$\langle \gamma_T(10-600'')\rangle$ $(\times 10^{-4})$	$\langle \gamma_R(10-600'')\rangle$ $(\times 10^{-5})$	η^{a}	$\gamma_{T0}{}^{\mathrm{a}}$ $(\times 10^{-5})$	$\mathrm{P}(>\chi^2)$	$\sigma_v{}^{\mathrm{a}}$ $(\mathrm{km\ s}^{-1})$	s^{a} (arcsec)	$\mathrm{P}(>\chi^2)$
g'	5.2 ± 0.77	7.3 ± 7.5	$0.73(0.70)$	$177(181)$	0.12	$153(155)$	$800(975)$	0.13
r'	5.8 ± 0.64	3.6 ± 6.4	$0.95(0.97)$	$272(268)$	0.03	$173(181)$	$250(200)$	0.02
i'	6.9 ± 0.65	-1.1 ± 6.5	$0.78(0.79)$	$254(252)$	0.54	$168(168)$	$675(700)$	0.59

[a]Values in parenthesis refer to fits to the shears with the systematics from Figure 5 subtracted.